Observation of three-dimensional massless Kane fermions in a zinc-blende crystal

M. Orlita[1,2]★, D. M. Basko[3], M. S. Zholudev[4,5], F. Teppe[4], W. Knap[4,6], V. I. Gavrilenko[5], N. N. Mikhailov[7], S. A. Dvoretskii[7], P. Neugebauer[8], C. Faugeras[1], A-L. Barra[1], G. Martinez[1] and M. Potemski[1]★

Solid-state physics and quantum electrodynamics, with its ultrarelativistic (massless) particles, meet in the electronic properties of one-dimensional carbon nanotubes, two-dimensional graphene or topological-insulator surfaces. However, clear experimental evidence for electronic states with a conical dispersion relation in all three dimensions, conceivable for certain bulk materials, is still missing. Here, we study a zinc-blende crystal, HgCdTe, at the point of the semiconductor-to-semimetal topological transition. For this compound, we observe three-dimensional massless electrons, as certified from the dynamical conductivity increasing linearly with the photon frequency, with a velocity of about 10^6 m s^{-1}. Applying a magnetic field B results in a $\sqrt{B}$-dependence of dipole-active inter-Landau-level resonances and spin splitting of Landau levels also following a $\sqrt{B}$-dependence—well-established signatures of ultrarelativistic particles but until now not observed experimentally in any solid-state electronic system.

The physics of 'Dirac cones', which largely dominates the research on electronic properties of one-dimensional (1D) and 2D allotropes of sp^2-bonded carbon[1–3] as well as topological insulators[4,5], is now anticipated to be also explored in 3D solids. Indeed, there have recently been a number of theoretical predictions of a class of fairly new materials with conical 3D electronic bands, such as Weyl semimetals (with an even number of momentum points where two conical bands touch) and Dirac semimetals (with one or more momentum points, in which four conical bands meet). Those compounds, such as the metastable β-cristobalite BiO$_2$ (ref. 6), pyrochlore iridates such as Y$_2$Ir$_2$O$_7$ (refs 7,8), A$_3$Bi where A is an alkali metal Na, K or Rb (ref. 9), distorted spinels[10], and TlBi(S$_{1-x}$Te$_x$)$_2$ and TlBi(S$_{1-x}$Se$_x$)$_2$ (ref. 11), will be possibly probed experimentally in the future, to clarify their bulk electronic structure. The surface states of the last compound have already been probed experimentally[12,13].

On the other hand, the presence of 3D conical dispersion relations of electronic states was suggested a long time ago[14] to be possible in more conventional, zinc-blende compounds known as narrow-gap semiconductors. On experimental ground, this particular shape of dispersion relations has not been seen as the main focus of studies so far. Nevertheless, a number of investigations, particularly in the 1960s and 1970s and including magneto-optical studies[15–19], have shown that the effective mass of the carriers and the energy bandgap in Hg$_{1-x}$Cd$_x$Te (MCT) can be made very small. The bandgap was estimated down to tens of milli-electron volts and the effective mass to 10^{-2} of the free-electron mass in samples with a cadmium concentration close to $x = 0.17$. This low effective mass could be a sign of linear dispersion relations, although the results of previous experiments might have been affected by insufficient sample quality (inhomogeneous chemical composition and high, unintentional doping), limiting their conclusiveness.

If the cadmium content is sufficiently high, $x > x_c \approx 0.17$, the MCT compounds are conventional (narrow-gap) semiconductors with the standard sequence of different symmetry bands: the s-type Γ_6 band is fixed above the p-type Γ_8 bands, as schematically shown in Fig. 1. Instead, if $x < x_c$, the band order is inverted: the Γ_6 band lies below the Γ_8 bands. As the two parabolic Γ_8 bands always touch each other at the Γ point of the first Brillouin zone, and only the lower band is occupied in the intrinsic case, for $x < x_c$ the band structure is gapless, and MCT becomes a semimetal. The two distinct phases are not topologically equivalent, as characterized by a Z_2 topological invariant[20]. At the point of the topological transition, when the cadmium concentration reaches its critical value, $x = x_c$, the bandgap shrinks to zero[19] and the electronic dispersion relation presents some very peculiar properties.

These conical bands have several spectacular properties similar to those in Dirac and Weyl semimetals (such as Klein tunnelling and suppressed backscattering, as discussed below). Nevertheless, a crucial difference must be stressed. Weyl semimetals are topologically protected; that is, the Weyl points are stable with respect to small perturbations. Dirac semimetals are not topologically protected, but can be protected by the crystal symmetry (that is, the Dirac points are stable with respect to perturbations that preserve this symmetry). The conical dispersion in the gapless MCT is not protected by symmetry or topology; rather, it is achieved by fine-tuning of a system parameter (cadmium concentration). The protected bands might be robust and then advantageously unaffected by small changes of external parameters. On the other hand, the band structure of MCT can be suitably engineered to
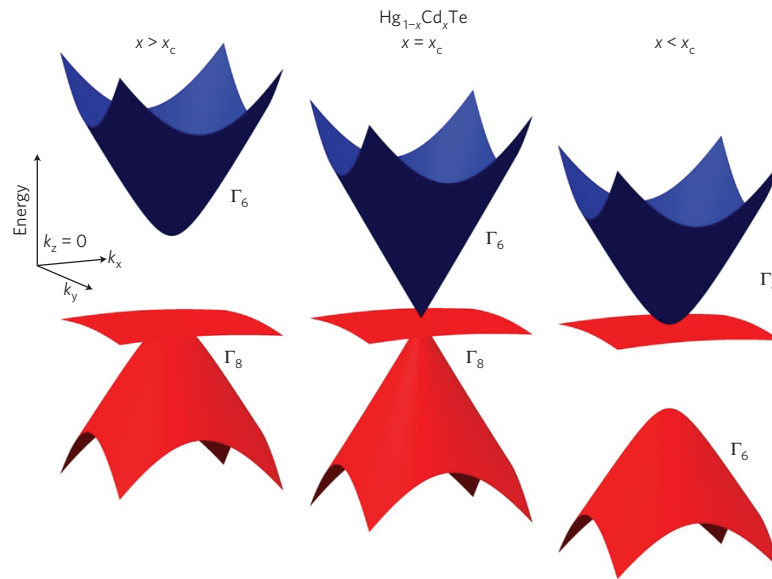
Figure 1 | Schematic band structure of MCT. The electronic dispersion of MCT at $k_z = 0$ for three different cadmium concentrations x. A standard gapped semiconductor for $x > x_c$ becomes a semimetal at $x < x_c$. At the point of the topological transition, $x = x_c$, the conduction band and the light-hole valence band have a 3D conical dispersion, which is crossed at the vertex by an almost flat heavy-hole band. In all parts, blue colour corresponds to the conduction band, and the valence bands are depicted in red.
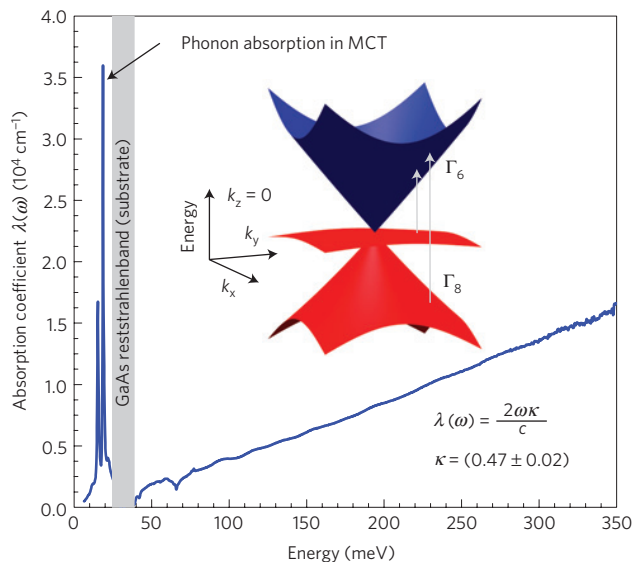

Figure 2 | Light absorption in MCT at zero magnetic field. Absorption coefficient of MCT at zero magnetic field, $\lambda_{B=0}$, measured experimentally as a function of photon energy (see the text and Methods for details). Whereas the low-energy response is dominated by absorption due to phonons, the linear dependence on ω at higher photon energies is directly linked to the conical dispersion of 3D massless fermions. The interband absorption in gapless MCT, schematically shown in the inset, is dominated by transitions from the flat (heavy-hole) band. The grey region corresponds to the GaAs reststrahlenband (substrate), where the investigated sample is fully opaque. Below this region, the absorption of phonons in MCT becomes dominant.

benefit the design and fabrication of 'gapped-at-will' compounds and their interfaces with massless systems.

The basic theoretical approach, needed to understand these properties, is based on the standard Kane model[21], whose validity for MCT has been confirmed by a number of previous studies[15–18], and which usually implies more than ten free parameters[19]. Here, we

retain only the terms linear in the wavevector, and neglect the split-off Γ_7 band (the magnitude of the splitting, $\Delta \approx 1$ eV (refs 19,22) is assumed to be sufficiently large). For the remaining six bands, the Hamiltonian can be written as (see Supplementary Information):

$$H(\mathbf{k}) = \begin{pmatrix} 0 & vk_+\sqrt{3}/2 & -vk_-/2 & 0 & 0 & -vk_z \\ vk_-\sqrt{3}/2 & 0 & 0 & 0 & 0 & 0 \\ -vk_+/2 & 0 & 0 & -vk_z & 0 & 0 \\ 0 & 0 & -vk_z & 0 & -vk_-\sqrt{3}/2 & vk_+/2 \\ 0 & 0 & 0 & -vk_+\sqrt{3}/2 & 0 & 0 \\ -vk_z & 0 & 0 & vk_-/2 & 0 & 0 \end{pmatrix} \equiv v\mathbf{k}\cdot\mathbf{J}$$

$$(1)$$

where $k_\pm = k_x \pm i k_y$, and the velocity $v = \sqrt{E_P/(3m_0)} \approx 10^6$ m s^{-1} is expressed in terms of the free-electron mass m_0 and the Kane energy E_P (typically, $E_P \approx 20$ eV for zinc-blende semiconductors; see, for example, ref. 23). The velocity is thus the only free parameter, which makes this model extremely simple.

The Hamiltonian (equation (1)) has three eigenvalues, each doubly degenerate owing to the Kramers theorem (time-reversal symmetry):

$$E_\mathbf{k} = 0, \pm v|\mathbf{k}|$$

As usual, the two components of the Kramers doublet can be labelled by two spin projections ↓, ↑, even though this degree of freedom has a strong admixture of the orbital motion due to the spin–orbit coupling. This implies an anomalously large and nonlinear Zeeman effect.

The eigenvalue $E_\mathbf{k} = 0$ corresponds to the heavy-hole band, which, in the approximation of equation (1), is dispersionless (completely flat) or, in other words, characterized by an infinite effective mass. The inclusion of parabolic terms in the electron dispersion results in a downward bending of the heavy-hole band, away from $\mathbf{k} = 0$. This curvature, corresponding to a heavy-hole mass of about $m_{hh} \approx 0.5 m_0$ (ref. 19), is not sensitive to the topological transition at $x = x_c$. The simplified picture of massless and infinite-mass particles can be used at sufficiently low energies E, such that the 'relativistic' mass of massless fermions, $m_c = E/v^2 \ll m_{hh}$. This defines the energy cutoff of $m_{hh}v^2 \approx 3$ eV, less stringent than the spin–orbit splitting $\Delta \approx 1$ eV. One step
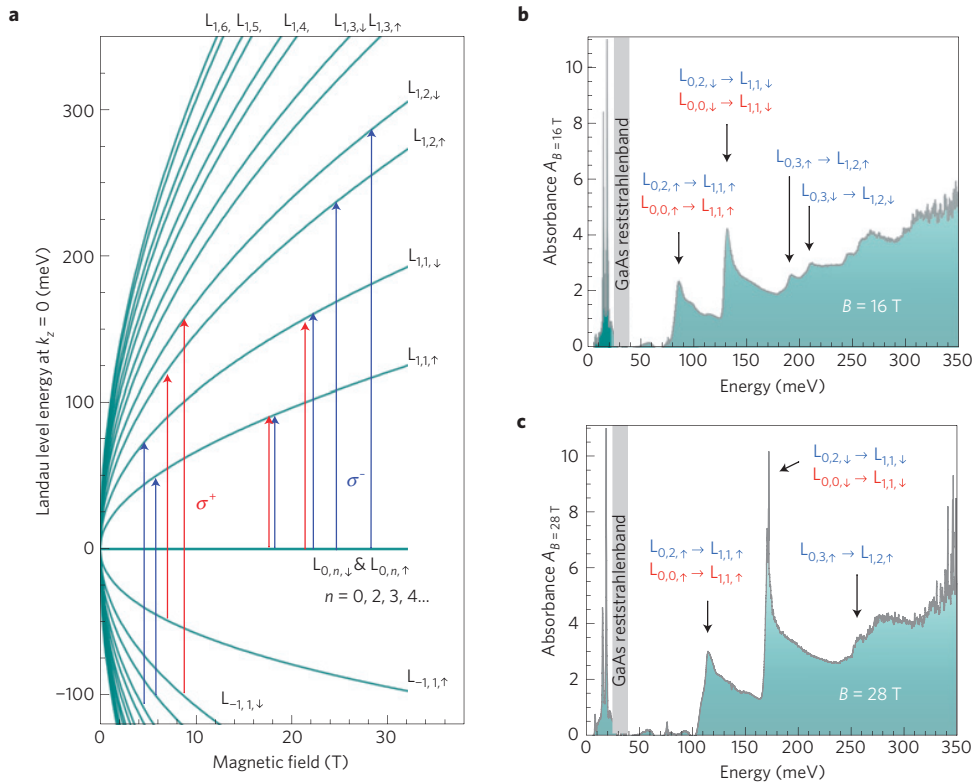
Figure 3 | Landau-level fan chart and magneto-absorption spectra of MCT. a, Landau levels (for $k_z = 0$) in gapless MCT, $L_{\zeta,n,\sigma}$, as a function of the magnetic field, calculated using the eight-band model, using only v and Δ as parameters. Arrows of different colours show the optically allowed transitions in undoped gapless MCT in the two circular polarizations σ^+ and σ^-. **b,c**, Experimentally measured absorption coefficient λ_B (absorbance) as a function of the photon energy, presented for two values of the magnetic field, $B = 16$ and 28 T, respectively.

beyond the approximation of equation (1) is therefore to use the eight-band model with a finite Δ though still ignoring the apparent dispersion of the heavy-hole band (see Supplementary Information for details). We follow such an approach when it is necessary to refine the analysis of the experimental data.

The matrices $\mathbf{J} = \{J_x, J_y, J_z\}$ that appear in equation (1) do not satisfy the algebra of angular momentum 1, nor any other closed algebra. Notably, the massless fermions in MCT are not equivalent to the 3D Dirac electrons in the ultrarelativistic limit of the quantum electrodynamics (QED). For example, the Hamiltonian in equation (1) has the characteristic property:

$$U_c H(\mathbf{k}) U_c = -H(\mathbf{k}), \quad U_c \equiv \text{diag}(1, -1, -1, 1, -1, -1) \quad (2)$$

Note, however, that in the above equation '−1' appears more often than '1'; hence, it is not the usual chiral property. As discussed in the Supplementary Information, the property (2) ensures the existence of a doubly degenerate flat band. To the best of our knowledge, the Hamiltonian (equation (1)) does not reduce to any well-known case of massless particles in QED. We therefore invoke a new term, Kane fermions, to refer to the electronic states of MCT at the point of the topological transition (to states in gapless MCT).

Massless Kane fermions share, however, a number of properties with other ultrarelativistic particles. A prominent example is Klein tunnelling invoked for 3D Dirac electrons in QED and apparent for 2D Dirac electrons in graphene[24,25]. A perfect transmission through an arbitrarily high potential barrier at normal incidence, due to the Klein paradox, should also occur in a gapless MCT. This can be seen by noting that the eigenstates corresponding to the same (for example, positive) energy but to opposite wavevectors $\mathbf{k}, -\mathbf{k}$, also correspond to different eigenvalues, ± 1, of the projection of $\mathbf{J}$ on $\mathbf{k}$. Thus, a potential that does not change $\mathbf{J}$ (such as the electrostatic

potential that acts in the same way on electrons in all bands and thus is proportional to the unit matrix), cannot backscatter an electron in the conduction band.

To prove the concept of massless Kane fermions in experiments, we have used the molecular beam epitaxy technique to grow thin layers of MCT on semi-insulating GaAs substrates (see Supplementary Information). The optimal structure was used for measurements. It contains an MCT layer with a cadmium concentration close to $x_{Cd} = 0.17$ that extends over a thickness of $d \approx 3.2\,\mu m$. The relevant part of this MCT layer is sufficiently thick to be considered a 3D material and at the same time thin enough to be suitable for our optical transmission experiments.

A striking consequence of conical dispersions on the optical properties of 3D massless fermions is the absorption coefficient $\lambda(\omega)$ being proportional to the frequency ω, distinctly in contrast to frequency-independent absorption of 2D Dirac electrons as observed in graphene[26,27]. In other words, these characteristic dependences result from the particular forms of the joint density of states $\mathcal{D}(\omega)$, which define the basic absorption profile in solids: $\lambda(\omega) \propto \mathcal{D}(\omega)/\omega$. A conical dispersion in 2D yields $\mathcal{D}(\omega) \propto \omega$, whereas it implies $\mathcal{D}(\omega) \propto \omega^2$ and thus $\lambda(\omega) \propto \omega$ in the case of a 3D system with massless particles.

To be more quantitative, we use a simple form of the Hamiltonian given by equation (1) and follow the standard recipe[23] to analytically derive the dielectric function $\varepsilon(\omega)$ of the system (see Supplementary Information). Defining Ω as the high-energy cutoff of the conical dispersion, one finds that if $\omega \ll \Omega$, then:

$$\varepsilon(\omega) = \varepsilon_\infty + \alpha \frac{13}{12} \frac{c}{v} \left(\frac{2}{\pi} \ln \frac{\Omega}{|\omega|} + i \, \text{sgn} \, \omega \right) \quad (3)$$

where α is the fine-structure constant ($\alpha \approx 1/137$) and ε_∞ accounts for the contribution from transitions other than those
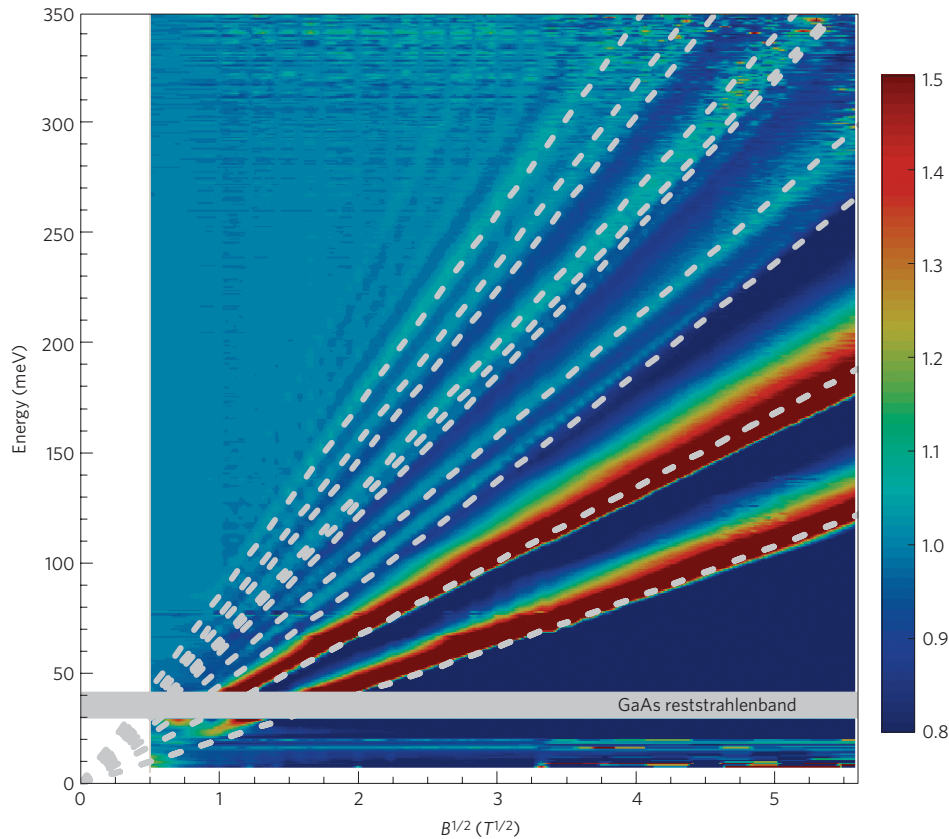
Figure 4 | Magneto-absorption in MCT. Relative change of absorbance $A_B/A_{B=0}$ plotted as a false-colour map. All of the observed resonances clearly follow a $\sqrt{B}$-dependence. The dashed lines are calculated positions of inter-Landau-level resonances at $k_z = 0$ using parameters $v_F = 1.06 \times 10^6$ m s^{-1} and $\Delta = 1$ eV. When the spin–orbit split band, accounted for by the parameter Δ, is taken into account, the Landau levels, and consequently the theoretically calculated inter-Landau level transitions, weakly deviate from the $\sqrt{B}$ dependence.

described by equation (1). Equation (3) is valid for the intrinsic material at zero temperature, $T = 0$. It has been noted recently[28,29] that in the intrinsic case (zero Fermi energy) the limits $\omega \to 0$ and $T \to 0$ do not commute. As discussed below, our sample is not fully intrinsic (some small residual population in the conduction band is present), so the limit $\omega \to 0$ is regularized by this residual population. The dissipative part of the dielectric function, Im$\varepsilon(\omega)$, is dispersionless, whereas Re$\varepsilon(\omega)$ gains a weak (logarithmic) dependence on ω. Consequently, we derive the dynamical conductivity, $\sigma(\omega) = i(1 - \varepsilon)\varepsilon_0 \omega$, the real part of which is a linear function of ω. Let us note that (interband) absorption in gapless MCT is dominated by transitions from the flat (heavy-hole) band, which is fully occupied in the intrinsic (undoped) material.

Equation (3) implies a nearly frequency-independent extinction coefficient $\kappa = \text{Im} \sqrt{\varepsilon(\omega)}$, and consequently, the absorption coefficient $\lambda(\omega)$ increasing linearly with ω, $\lambda(\omega) = (2\kappa\omega)/c$. The experimentally observed value $\kappa = 0.47 \pm 0.02$ derived directly from the data shown in Fig. 2 agrees fairly well with the extinction coefficient, $\kappa \approx 0.4$, calculated using equation (3) (see Methods for more details).

In a strong magnetic field, the 3D dispersion is transformed into a set of Landau levels, or more precisely, into 1D Landau bands that disperse with the momentum component along the field (z axis). Inserting the magnetic field into the Hamiltonian in equation (1) through the standard Peierls substitution, $\hbar \mathbf{k} \to \hbar \mathbf{k} - e\mathbf{A}$, one obtains for gapless MCT the Landau-level energies (see Supplementary Eq. (28)):

$$E_{\zeta,n,\sigma}(k_z) = \zeta \hbar v \sqrt{(2n - 1 + \sigma/2) l_B^{-2} + k_z^2} \qquad (4)$$

where $l_B^{-2} = eB/\hbar$ and the Landau-level index $n = 0, 1, 2...$. For $n \geq 2$, the band index is $\zeta = 1, 0, -1$, whereas at $n = 1$ only $\zeta = \pm 1$ are allowed and at $n = 0$ only $\zeta = 0$ exists. The states in the flat band remain at zero energy, because the property (2) remains valid in the presence of a magnetic field.

The quantum number $\sigma = \pm 1$ shows how the Kramers degeneracy, mentioned above, is lifted by the magnetic field. Thus, σ can be viewed as the spin projection on the magnetic field. The spin splitting is entirely determined by the orbital parameters v, n and k_z. Moreover, at $k_z = 0$ the spin splitting of all Landau levels is proportional to $\sqrt{B}$, which means that the g factor defined in the standard way, $g_{\zeta,n} = (E_{\zeta,n,\uparrow} - E_{\zeta,n,\downarrow})/(\mu_B B)$, diverges at $B \to 0$. This is quite unusual for a solid-state system, and, in particular, does not hold for the Dirac fermions in graphene. On the other hand, such behaviour is characteristic of ultrarelativistic Dirac electrons in QED, $E_{\zeta,n,\sigma}(k_z) = \zeta \hbar c \sqrt{(2n + 1 + \sigma)/l_B^2 + k_z^2}$, where $n = 0, 1...$ and $\zeta = \pm 1$ (see, for example, ref. 30). Note, however, an essential difference: in QED, a level $(n, \sigma = +1)$ is degenerate with the level $(n + 1, \sigma = -1)$. Such degeneracy is absent for Kane fermions, because it is $\sigma/2$ that enters equation (4). The $\sqrt{B}$ spin splitting occurs in MCT because the strength of the spin–orbit coupling becomes effectively infinite when the energy gap vanishes. Let us now discuss how the $\sqrt{B}$-dependence of Landau levels and also of the spin splitting at $k_z = 0$, described by equation (4), is verified experimentally.

The magneto-optical response of MCT is determined by electric-dipole selection rules: $\Delta n = n \pm 1$ with '$\pm$' corresponding to the two circular polarizations, $\Delta k_z = 0$, $\Delta \sigma = 0$, and no restriction on ζ. In the undoped MCT, the incident photon can excite electrons from the filled valence bands, $\zeta = -1, 0$, to the empty conduction band, $\zeta = 1$, as shown schematically in Fig. 3a. Examples of the measured
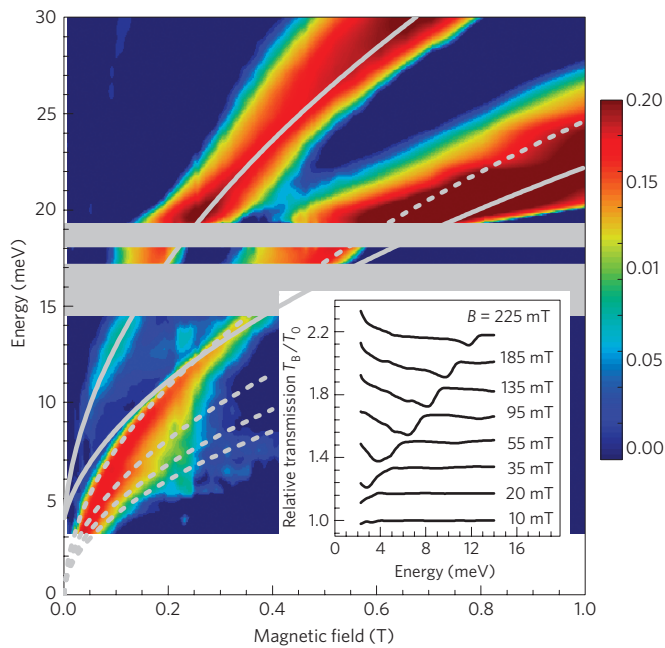
Figure 5 | Low-field magneto-transmission in MCT. Relative change of transmission, plotted as $-\ln(T_B/T_0)$, in the form of a colour map at low fields. The inset shows selected transmission spectra, in which the well-defined cyclotron resonance response is observed down to 30 mT. The solid and dashed lines correspond to expected positions of inter-Landau-level transition in a MCT system with $v = 1.06 \times 10^6$ m s^{-1} and a small energy gap of $E_g = 4$ meV. The solid lines show the two lowest-lying interband resonances (from the flat band to $L_{1,1,\uparrow}$ and $L_{1,1,\downarrow}$ levels); the dashed lines are pure cyclotron-resonance-like transitions between pairs of adjacent Landau levels in the conduction band ($\zeta = 1, n = 1, 2, 3 \dots$). The grey areas correspond to regions of strong phonon-related absorption in MCT.

spectra are shown in Fig. 3b. As the dispersion of each Landau band near $k_z = 0$ is parabolic, the joint density of states has sharp inverse-square-root singularities at energies of the transitions with $k_z = 0$, with an abrupt cutoff on the low-energy side and a shoulder on the high-energy side, as expected also for Weyl semimetals[31]. In the absence of a magnetic field, such a density of states can be found in 1D Dirac-type systems, in particular, in carbon nanotubes[1]. Note that the singularity of the lowest transition is less sharp than that of the next one. We attribute this to a small residual electronic doping, which results in filling of the states with very small k_z in the lowest Landau level in the conduction band ($L_{1,1,\uparrow}$), so that the optical transition involving these states is blocked by the Pauli principle, thereby cutting off the singularity.

The key feature of the massless fermions, expressed by equation (4), is the $\sqrt{B}$-dependence of the transition energies at $k_z = 0$. In Fig. 4, we plot the infrared absorbance spectrum (relative to the zero-field absorbance) for magnetic fields up to 31 T. When plotted as a function of $\sqrt{B}$, the positions of the $k_z = 0$ singularities guide the eye along straight lines. A close inspection shows that they are slightly curved at high fields. This weak curvature can be accounted for by including the spin–orbit split-off band with $\Delta = 1$ eV. The theoretical curves in Fig. 4 were produced using such an eight-band model, considering v_F and Δ as the only two parameters. The two brightest lines correspond to the transitions from the flat band to the two spin-split components of the first Landau level in the conduction band (levels $L_{1,1,\uparrow}$ and $L_{1,1,\downarrow}$; Fig. 3a). This agreement between experiment and theory provides us with another fingerprint of 3D massless fermions in gapless MCT. Let us note that the $\sqrt{B}$-dependence does not serve as a unique signature

of 3D massless particles and it can be found, for a certain range of magnetic fields, in the optical response of other bulk materials, for example, in highly anisotropic graphite and bismuth[32–34].

Having shown that in a wide, 30–300 meV, energy range, the optical response of our sample is well explained by a model of gapless and intrinsic (undoped) MCT, we focus now on the low-energy, low-magnetic-field range (Fig. 5) of our data, with the aim of estimating the accuracy of such an approach. The spectral range of interest, below 30 meV, is not easy to explore because of strong phonon contributions to the absorption, which mask the evolution of electronic resonances. Nevertheless, a slight deviation of the experimental data from a model of an ideal, gapless and intrinsic MCT becomes apparent.

First, we concentrate on two, most pronounced interband transitions in the region around 25 meV and conclude that they appear at higher energies than those expected from simple calculations using equation (4). This discrepancy points towards an MCT with a small but still non-zero gap E_g. Setting $E_g = 4$ meV in calculations we satisfactorily improve the data modelling (Fig. 5, solid lines).

The second relevant observation is that the interband transitions, which are strong at higher energies, rather suddenly weaken in the limit of low magnetic fields. At the same time, the lowest-energy interband transition transforms into a resonance that follows a linear rather than $\sqrt{B}$-dependence in small magnetic fields. These effects indicate that our structure is not perfectly intrinsic but characterized by a non-zero electron concentration (Fermi energy E_F in the conduction band). Indeed, if the electron concentration is not zero, each interband Landau-level transition must be (Pauli) blocked at sufficiently low fields, when the corresponding electronic Landau level crosses below the Fermi energy. Our interband transitions are barely seen at energies below 15 meV, Fig. 5. This allows us to estimate $E_F \approx 15$–17 meV, and in consequence also the electron concentration $n = (1/3\pi^2 v^3 \hbar^3)[E_F(E_F - E_g)]^{3/2} = (2-3) \times 10^{14}$ cm^{-3} (for $E_g = 4$ meV estimated above).

The presence of free electrons in our structure explains also its spectral response at low energies (below 15 meV). This response is due to classical cyclotron resonance absorption at low magnetic fields, which transforms with increasing B into intraband transitions between adjacent Landau levels and ends up as a transition from the flat band into the $L_{1,1,\uparrow}$ level (Fig. 3a) when E_F is locked at the bottom of the $L_{1,1,\uparrow}$ level. It is worth noting that, independently of parabolic or linear electronic dispersions, the classical cyclotron resonance is linear with the magnetic field, invoking a $m_c = E_F/v^2$ effective mass in the case of linear dispersion relations[35–37]. In our case, a small gap is present and the cyclotron mass becomes $m_c = (E_F - E_g/2)/v^2 \approx 2 \times 10^{-3} m_0$. This value corresponds well to the cyclotron mass, $m_c = (1.5 \pm 0.5) \times 10^{-3} m_0$ derived directly from the slope of cyclotron resonance absorption in the limit of low magnetic fields.

In conclusion, we have observed a new type of 3D massless fermions, which extend the known family of 3D massless particles. These 'Kane fermions' share many features with previously discussed Weyl and Dirac fermions: optical absorption that is linear in frequency, Landau levels and their Zeeman splitting, which are proportional to $\sqrt{B}$ and rigidly related to each other. However, the relation between the spin and orbital splitting for massless Kane fermions is different from that for the ultrarelativistic Dirac electrons or Weyl fermions, which is one manifestation of their inequivalence. An important difference from massless electrons in Weyl semimetals is that the massless fermions in MCT are not protected by symmetry or topology; rather, we have engineered the conical dispersion by fine-tuning a system parameter, cadmium concentration, which is extremely homogeneous over a macroscopic thickness. This lack of protection, in fact, may represent a major advantage for potential applications: the very robust nature of semimetals protected by symmetry or topology makes them hard

to manipulate (for example, to introduce a small controllable gap), whereas the band structure of the MCT can be engineered at will, as our work shows. The high degree of technological control over this material opens further perspectives for its use in electronic devices, where one could benefit from the peculiar properties of massless fermions, such as the suppressed backscattering (Klein paradox) and the related inefficient Auger-type recombination.

While our paper was under review, we have learned about several recent preprints[38–40], where related issues are discussed.

Methods

The sample was grown using standard molecular-beam epitaxy on a (013)-oriented semi-insulating GaAs substrate. The growth sequence started with ZnTe and CdTe transition regions, followed by the MCT epilayer with gradually changing cadmium content x (see Supplementary Information). The prepared MCT layer contains a region with $x \approx 0.17$ of thickness $d \approx 3.2\,\mu m$.

The absorption coefficient of MCT was measured in the transmission configuration. A macroscopic area of the sample of about $4\,mm^2$ was exposed to the radiation of a globar or mercury lamp, which was analysed by a Fourier transform spectrometer, and using light-pipe optics delivered to the sample placed either in a superconducting solenoid or resistive coil. At low fields, the correction for the remanent field of the solenoid has been made. The transmitted light was detected by a composite bolometer placed directly below the sample, kept at a temperature of 1.8 K. The sample transmission T_B at a given magnetic field B was normalized by the substrate transmission, T_S, measured in the absence of MCT. The absorption coefficient λ_B was determined from the relation $T_B/T_S = \exp(-\lambda_B d)$. This relation neglects the dielectric mismatch between MCT and GaAs. A significant mismatch would result in additional reflection and would produce a constant vertical shift of the curve in Fig. 2, so the straight line would not pass through the origin. The fact that it does, shows that the dielectric mismatch is indeed negligible. This implies $\varepsilon_\infty \approx 6$, when the realistic cutoff energy $\Omega = 1.5$ eV is assumed[41].

References

1. Charlier, J-C., Blase, X. & Roche, S. Electronic and transport properties of nanotubes. *Rev. Mod. Phys.* **79,** 677–732 (2007).
2. Novoselov, K. S. *et al.* Two-dimensional gas of massless Dirac fermions in graphene. *Nature* **438,** 197–200 (2005).
3. Zhang, Y. B., Tan, Y. W., Stormer, H. L. & Kim, P. Experimental observation of the quantum Hall effect and Berrys phase in graphene. *Nature* **438,** 201–204 (2005).
4. König, M. *et al.* Quantum spin Hall insulator state in HgTe quantum wells. *Science* **318,** 766–770 (2007).
5. Hasan, M. Z. & Kane, C. L. Colloquium: Topological insulators. *Rev. Mod. Phys.* **82,** 3045–3067 (2010).
6. Young, S. M. *et al.* Dirac semimetal in three dimensions. *Phys. Rev. Lett.* **108,** 140405 (2012).
7. Wan, X., Turner, A. M., Viswanath, A. & Savrasov, S. Y. Topological semimetal and Fermi-arc surface states in the electronic structure of pyrochlore iridates. *Phys. Rev. B* **83,** 205101 (2011).
8. Yang, K-Y., Lu, Y-M. & Ran, Y. Quantum Hall effects in a Weyl semimetal: Possible application in pyrochlore iridates. *Phys. Rev. B* **84,** 075129 (2011).
9. Wang, Z. *et al.* Dirac semimetal and topological phase transitions in A_3Bi (A = Na, K, Rb). *Phys. Rev. B* **85,** 195320 (2012).
10. Steinberg, J. A. *et al.* Bulk Dirac points in distorted spinels. Preprint at http://arxiv.org/abs/1309.5967 (2013).
11. Singh, B. *et al.* Topological electronic structure and Weyl semimetal in the TlBiSe$_2$ class of semiconductors. *Phys. Rev. B* **86,** 115208 (2012).
12. Xu, S-Y. *et al.* Topological phase transition and texture inversion in a tunable topological insulator. *Science* **332,** 560–564 (2011).
13. Sato, T. *et al.* Unexpected mass acquisition of Dirac fermions at the quantum phase transition of a topological insulator. *Nature Phys.* **7,** 840–844 (2011).
14. Zawadzki, W. Electron transport phenomena in small-gap semiconductors. *Adv. Phys.* **23,** 435–522 (1974).
15. Harman, T. C. *et al.* Low electron effective masses and energy gap in Cd$_x$Hg$_{1-x}$Te. *Phys. Rev. Lett.* **7,** 403–405 (1961).
16. McCombe, B. D., Wagner, R. & Prinz, G. Infrared pulsed gas laser studies of combined resonance and cyclotron–phonon resonance in Hg$_{1-x}$Cd$_x$Te. *Solid State Commun.* **8,** 1687–1691 (1970).
17. Groves, S. H., Harman, T. C. & Pidgeon, C. R. Interband magnetoreflection of Hg$_{1-x}$Cd$_x$Te. *Solid State Commun.* **9,** 451–455 (1971).
18. Guldner, Y., Rigaux, C., Mycielski, A. & Couder, Y. Magnetooptical investigation of Hg$_{1-x}$Cd$_x$Te mixed crystals II. Semiconducting configuration and semimetal → semiconductor transition. *Phys. Status Solidi* **82,** 149–158 (1977).
19. Weiler, M. H. in *Defects, (HgCd)Se, (HgCd)Te* (eds Willardson, R. K. & Beer, A. C.) 119–191 (Semiconductors and Semimetals, Vol. 16, Elsevier, 1981).
20. Bernevig, B. A., Hughes, T. L. & Zhang, S-C. Quantum spin Hall effect and topological phase transition in HgTe quantum wells. *Science* **314,** 1757–1761 (2006).
21. Kane, E. O. Band structure of indium antimonide. *J. Phys. Chem. Solids* **1,** 249–261 (1957).
22. Novik, E. G. *et al.* Band structure of semimagnetic Hg$_{1-y}$Mn$_y$Te quantum wells. *Phys. Rev. B* **72,** 035321 (2005).
23. Yu, P. Y. & Cardona, M. *Fundamentals of Semiconductors* (Springer, 1996).
24. Katsnelson, M. I., Novoselov, K. S. & Geim, A. K. Chiral tunnelling and the Klein paradox in graphene. *Nature Phys.* **2,** 620–625 (2006).
25. Young, A. F. & Kim, P. Quantum interference and Klein tunnelling in graphene heterojunctions. *Nature Phys.* **5,** 222–226 (2009).
26. Kuzmenko, A. B. *et al.* Universal optical conductance of graphite. *Phys. Rev. Lett.* **100,** 117401 (2008).
27. Nair, R. R. *et al.* Fine structure constant defines visual transparency of graphene. *Science* **320,** 1308 (2008).
28. Burkov, A. A. & Balents, L. Weyl semimetal in a topological insulator multilayer. *Phys. Rev. Lett.* **107,** 127205 (2012).
29. Goswami, P. & Chakravarty, S. Quantum criticality between topological and band insulators in 3+1 dimensions. *Phys. Rev. Lett.* **107,** 196803 (2011).
30. Berestetskii, V. B., Lifshitz, E. M. & Pitaevskii, L. P. *Relativistic Quantum Theory* (A Course of Theoretical Physics, Vol. 4, part 1, Pergamon, 1971).
31. Ashby, P. E. C. & Carbotte, J. P. Magneto-optical conductivity of Weyl semimetals. *Phys. Rev. B* **87,** 245131 (2013).
32. Maltz, M. & Dresselhaus, M. S. Magnetoreflection studies in bismuth. *Phys. Rev. B* **2,** 2877–2887 (1970).
33. Zhu, Z. *et al.* Angle-resolved Landau spectrum of electrons and holes in bismuth. *Phys. Rev. B* **84,** 115137 (2011).
34. Orlita, M. *et al.* Dirac fermions at the H point of graphite: Magnetotransmission studies. *Phys. Rev. Lett.* **100,** 136403 (2008).
35. Witowski, A. M. *et al.* Quasiclassical cyclotron resonance of Dirac fermions in highly doped graphene. *Phys. Rev. B* **82,** 165305 (2010).
36. Crassee, I. *et al.* Giant Faraday rotation in single- and multilayer graphene. *Nature Phys.* **7,** 48–51 (2011).
37. Orlita, M. *et al.* Classical to quantum crossover of the cyclotron resonance in graphene: A study of the strength of intraband absorption. *New J. Phys.* **14,** 095008 (2012).
38. Neupane, M. *et al.* Observation of a topological 3D Dirac semimetal phase in high-mobility Cd$_3$As$_2$. Preprint at http://arxiv.org/abs/1309.7892 (2013).
39. Borisenko, S. *et al.* Experimental realization of a three-dimensional Dirac semimetal. Preprint at http://arxiv.org/abs/1309.7978 (2013).
40. Liu, Z. K. *et al.* Discovery of a three-dimensional topological Dirac semimetal, Na$_3$Bi. Preprint at http://arxiv.org/abs/1310.0391 (2013).
41. Hass, K. C., Ehrenreich, H. & Velický, B. Electronic structure of Hg$_{1-x}$Cd$_x$Te. *Phys. Rev. B* **27,** 1088–1100 (1983).

Author contributions

The experiment was proposed by M.O. and M.P.; the underlying theory was formulated by D.M.B. The sample growth was performed by N.N.M. and S.A.D. The sample was characterized by M.S.Z., F.T., W.K. and V.I.G. Magneto-optical experiments were performed by M.O., G.M., M.S.Z., P.N., C.F. and A-L.B. All coauthors discussed the data. M.O., M.P. and D.M.B. wrote the manuscript.

Additional information

Supplementary information is available in the online version of the paper. Reprints and permissions information is available online at www.nature.com/reprints. Correspondence and requests for materials should be addressed to M.O. or M.P.

Competing financial interests

The authors declare no competing financial interests.